Nanomanufacturing and Metrology (2024) 7:6
https://doi.org/10.1007/s41871-024-00225-w

ORIGINAL ARTICLE

Systematic Radio Telescope Alignment Using Portable Fringe Projection Profilometry

Joel Berkson[1] · Justin Hyatt[2] · Nathan Julicher[2] · Byeongjoon Jeong[1] · Isaac Pimienta[2] · Rachel Ball[2] · Wyatt Ellis[2] · Jason Voris[2] · Diego Torres-Barajas[1,2] · Daewook Kim[1,2]

Received: 25 November 2023 / Revised: 14 February 2024 / Accepted: 15 February 2024 / Published online: 15 March 2024
© The Author(s) 2024

Abstract

In 2019, the Event Horizon Telescope (EHT) released the first-ever image of a black hole event horizon. Astronomers are now aiming for higher angular resolutions of distant targets, like black holes, to understand more about the fundamental laws of gravity that govern our universe. To achieve this higher resolution and increased sensitivity, larger radio telescopes are needed to operate at higher frequencies and in larger quantities. Projects like the next-generation Very Large Array (ngVLA) and the Square-Kilometer Array (SKA) require building hundreds of telescopes with diameters greater than 10 ms over the next decade. This has a twofold effect. Radio telescope surfaces need to be more accurate to operate at higher frequencies, and the logistics involved in maintaining a radio telescope need to be simplified to support them properly in large quantities. Both of these problems can be solved with improved methods for surface metrology that are faster and more accurate with a higher resolution. This leads to faster and more accurate panel alignment and, therefore, a more productive observatory. In this paper, we present the use of binocular fringe projection profilometry as a solution to this problem and demonstrate it by aligning two panels on a 3-m radio telescope dish. The measurement takes only 10 min and directly delivers feedback on the tip, tilt, and piston of each panel to create the ideal reflector shape.

Highlights

1. Current methods for measuring and aligning radio telescope dishes are insufficient for future astronomy requirements.
2. We've developed a 3D scanning method for measuring full aperture dishes outdoors that is faster, easier, and more reliable than current methods.
3. We demonstrated the method by aligning two panels on a 3-m dish to a high accuracy.

Keywords Metrology · Fringe projection profilometry · Off-axis alignment · Radio astronomy · Radio antenna

1 Introduction

Radio astronomy is used to observe the night sky through a lens different from the one used in optical astronomy, able to see the unseen. The manufacturing paradigms are also significantly different. In radio astronomy, direct recording of radio wave phase information can be done for GHz frequencies, meaning that signals from radio telescopes separated by great distances can be correlated in post-processing to achieve angular resolution far better than optical telescopes. This is clearly demonstrated by the images of black hole event horizons taken by the Event Horizon Telescope (EHT)

✉ Justin Hyatt
justinjh@arizona.edu

[1] James C. Wyant College of Optical Sciences, University of Arizona, 1630 E. University Blvd., Tucson, AZ 85721, USA

[2] Department of Astronomy at Steward Observatory, University of Arizona, 933 N Cherry Ave., Tucson, AZ 85721, USA

with micro-arcsecond resolution [1, 2]. The use of longer wavelengths in radio astronomy proportionally loosens the accuracy requirements of the main reflector relative to those for optical astronomy. The trade-off is that much larger reflectors are required to obtain a good signal-to-noise (SNR) ratio, as radio signals are typically weaker than optical. It is well known that optical telescopes scale cost with aperture diameter at approximately $D^{2.77}$. Fortunately, the cost of radio telescopes tends to scale at a rate closer to D^2, increasing linearly with the collecting area [3, 4]. As radio telescopes aim to achieve ever-higher resolutions, higher frequencies are required; thus, tighter requirements are imposed on the primary reflector. The Ruze equation describes how the surface root mean square (RMS) error of the reflector affects the antenna gain, where G_0 is the nominal gain considering a perfect reflector, ϵ is the surface RMS, and λ is the wavelength expressed in the same physical units [5].

$$G(\epsilon) = G_0 e^{\frac{4\pi\epsilon}{\lambda}^2} \tag{1}$$

Figure 1 shows the antenna gain degradation as a function of the RMS-to-wavelength ratio. A common bare minimum performance goal is to achieve a 3 dB loss (50%), which correlates to $\approx \lambda/15$. For example, the EHT observes a 1.3 mm wavelength at 230 GHz. Thus, to preserve antenna gain, the surface must meet ≈ 85 µm RMS. This RMS value includes the stack-up error from the individual panel accuracy, gravity deformations, temperature gradients, wind shake, and panel misalignment [6]. Panel alignment and adjustment are critical to deploying a radio telescope for optimal gain. The manufacturing cost associated with making accurately shaped panels is wasted if they are not properly aligned. If the status of panel-to-panel alignment and panel deformation is not known, adjustments cannot be made.

Common methods for measuring panel alignment and shape have historically included photogrammetry [7–10], holography [11–14], and laser trackers or laser trusses [10, 15–17]. Oftentimes, a combination of methods is used [10, 18–20]. All of these methods deliver the information on the surface accuracy of a dish, but they have many fundamental limitations and drawbacks. The spatial sampling of photogrammetry and laser trackers is limited to the number of fiducials or manually scanned points. The manual nature of these methods makes them time-consuming and expensive, requiring large teams of researchers to execute the metrology. The University of Arizona recently tuned the alignment of dish panels in a 12-m diameter radio telescope using photogrammetry. It required a team of three (scientists and engineers) to work for two weeks. The accuracy of these methods also degrades with working distance, so as aperture size increases, depth resolution decreases. For extremely large apertures that observe with millimeter wavelengths, holography has been the default method for measuring reflector deformations. Holography uses a smaller dish (that is assumed to be perfect) pointed at a satellite beacon (typically a geosynchronous satellite to avoid the need for tracking) as a reference signal. The antenna under test then raster scans across the source to sample the beam [21, 22]. Correlations with the reference signal are used to recover the absolute phase errors, and inverse Fourier transforms are used to recover the aperture wavefront error, which feeds back to required surface adjustments to make corrections. While holography is known to have great sensitivity, it is limited in logistics. Specialized cryogenic detectors designed to match the frequency of the geosynchronous satellite beacon are required to take measurements. Also, because of the use of geosynchronous satellites, only one elevation angle can be tested, meaning gravitational deformations at other elevation angles remain unknown. The measurements are time-consuming because of the need to raster scan the entire telescope to sample the beam, and good environmental conditions are required for successful measurements. The algorithms to determine adjustments on the primary reflector vary widely from telescope to telescope depending on the size, on-axis versus off-axis configuration, and the presence of secondary or tertiary reflectors. Many future plans for large radio telescopes involve multiple off-axis reflectors [23–26].

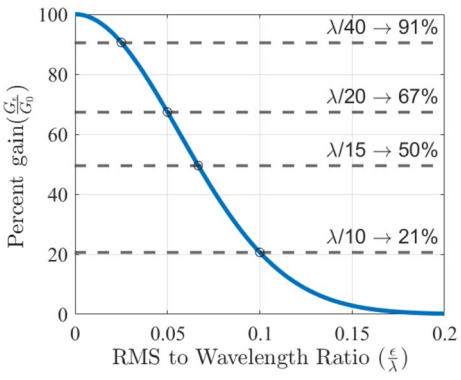

Fig. 1 Plotting the percent gain dictated by the Ruze Equation as a function of the surface RMS to wavelength ratio. At $\lambda/15$, a 3 dB loss, or 50%, is achieved

Regardless of the current metrology method used on a radio antenna dish, there are drawbacks in cost, time, logistics, and data quality. Oftentimes, the use of multiple methods is required. In 2022, our research group developed a metrology technique based on binocular fringe projection profilometry for measuring radio telescope panels in a laboratory setting to assist our research into the rapid fabrication of radio telescope panels [27]. As a demonstration of the panel forming technique, our research team is constructing a 2.4 m × 3.2 m radio telescope, known as the Student Radio Telescope (SRT), using our own fabricated panels [28]. The

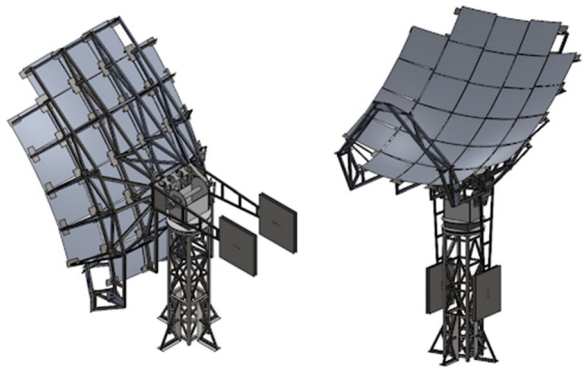

Fig. 2 3D rendering of the SRT. The telescope will consist of 26 500 mm × 500 mm panels, each with a different shape due to the off-axis paraboloid design

problem of aligning the panels has driven the team to adapt the previously developed panel metrology method to be portable, function outdoors, measure discontinuous objects, and cover large areas with high resolution. As a demonstration, we will show in this paper how the system can be used to deliver alignment feedback information for two adjacent panels on the SRT. The telescope is currently under construction for the purpose of public outreach. Figure 2 shows a 3D rendering of the SRT.

2 Background

Before installing and aligning panels on a radio telescope, panels are manufactured and measured in a factory. Typically, Coordinate Measuring Machines (CMMs) are used to perform metrology on these surfaces to ensure they meet the required accuracy. However, as panels approach one or even two meters in size, CMMs become more costly, and data collection becomes very slow. In 2022, our team developed a technique for measuring panels and panel molds with a modification to fringe projection profilometry (FPP) [27]. The method uses two calibrated cameras (using Zhang's method [29]) as a stereo pair and a DLP projector. Figure 3 shows the current system based in the lab for measuring the mold and the panels. The projector displays a series of phase-stepped fringe patterns in vertical and horizontal directions onto a unit under test (UUT). The N-step phase shifting algorithm [30] is used to recover the wrapped phase of the patterns. The phase is then unwrapped using a spatial phase unwrapping method [31]. The resulting horizontal and vertical phase combination is unique for every projector pixel, and as a result, the series of patterns encodes the UUT with unique phase pairs. These phase pairs are used as fiducials to find matching points in the images captured by the two cameras. The calibrated intrinsic and extrinsic parameters of the stereo pair are used to triangulate the set

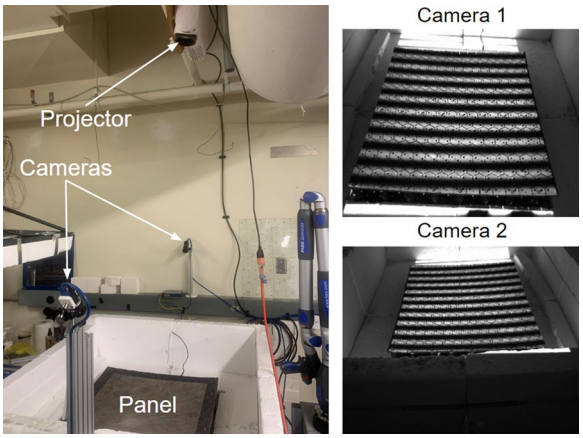

Fig. 3 Binocular FPP system in a laboratory setting. The system is used for measuring a flexible mold and measuring the panels that are thermally formed to it

of matching points to produce a 3D point cloud relative to the perspective of camera 1 [32]. Conventional FPP uses one camera and one projector to directly convert phase to height, so the measurement sensitivity is dependent on the chief ray angle between the projector and the camera. Since phase in this system is used only as a matching fiducial, the measurement sensitivity is dependent on the chief ray angle between the stereo cameras rather than between the camera and the projector. The nature of this method allows nearly every pixel that falls on the object to be converted into a 3D point.

3 Methods

3.1 Binocular Fringe Projection Profilometry with Hierarchical Unwrapping

The previously described method does not work for discontinuous surfaces as the spatial phase unwrapping for a single frequency produces only a relative phase, not an absolute phase. As a result, there is an integer multiple of 2π phase ambiguity between discontinuous objects, for example, two adjacent panels in a radio telescope, when using a spatial phase unwrapping method. To ensure reliable and absolute phase unwrapping, we have implemented a temporal phase unwrapping technique known as hierarchical, or multifrequency, phase unwrapping [33]. The method uses an initial low-frequency fringe period so that less than one period covers the entire span of the projected area, so it has no 2π phase ambiguity. Increasingly higher frequencies are applied, with the lower frequency used to unwrap the next highest frequency, as in Eq. (2).

$$k_n(x,y) = \text{Round}\left(\frac{\frac{\lambda_{n-1}}{\lambda_n}\phi_{n-1}(x,y) - \phi_n(x,y)}{2\pi}\right) \tag{2}$$

$$\Phi_n(x,y) = \phi_n(x,y) + 2\pi k_n(x,y) \tag{3}$$

In Eq. (2), n indicates the frequency being used from lowest to highest. $k_n(x,y)$ is the map of fringe orders used to unwrap $\phi_n(x,y)$ to create the unwrapped map, $\Phi_n(x,y)$, for fringe period λ_n. The round(.) function rounds the argument to the nearest integer, with steps of 0.5 rounded up to the next highest integer. The process of Eqs. (2) and (3) is done iteratively until the final highest frequency or shortest fringe period is reached. We used 5-step phase shifts for each fringe period of 1920, 500, 100, and 10 pixels. Fringe period 1920 matches the widest screen dimension for 1080P projectors, producing no unwrapping ambiguity. In theory, only the lowest frequency and the highest frequency are needed, but in the presence of noise and imperfect fringe patterns, using multiple frequencies helps ensure proper identification of fringe orders for unwrapping each consecutive frequency [34].

3.2 Dish Measurement with Global Reference Frame

As mentioned in the Introduction, this stereo camera FPP system returns 3D data points relative to one of the camera axes. This is sufficient to align panels to one another to make the smoothest surface, but this surface needs to focus incoming radio signals on a known position. The SRT is an off-axis paraboloidal design with a direct feed. To ease the process of determining a global reference frame, two circular fiducials are included in the FPP measurement of the field of view of the SRT to define the optical axis of the telescope, one at the paraboloid vertex and another at the desired focal point.

These two fiducials will also be identified and triangulated in the stereo camera system, returning two 3D points relative to camera 1: $\boldsymbol{P}_{\text{vertex}} = (X_{\text{vertex}}, Y_{\text{vertex}}, Z_{\text{vertex}})$ and $\boldsymbol{P}_{\text{focus}} = (X_{\text{focus}}, Y_{\text{focus}}, Z_{\text{focus}})$. Their centers are identified using the Hough transform [35, 36]. We perform the following coordinate transformations to orient the measured panels ($\boldsymbol{P}_{\text{panel}} = (\boldsymbol{X}_{\text{panel}}, \boldsymbol{Y}_{\text{panel}}, \boldsymbol{Z}_{\text{panel}})$) to the optical axis and the paraboloidal equation. Then, we extract the required rigid body motions for each panel to obtain the lowest RMS surface error.

1. Translate the entire map to locate $\boldsymbol{P}_{\text{vertex}}$ at the origin.

$$\begin{aligned}\boldsymbol{P}'_{\text{panel}} &= \boldsymbol{P}_{\text{panel}} - \boldsymbol{P}_{\text{vertex}}\\ \boldsymbol{P}'_{\text{focus}} &= \boldsymbol{P}_{\text{focus}} - \boldsymbol{P}_{\text{vertex}}\end{aligned} \tag{4}$$

2. Calculate Euler angles α and β of the line that connects the vertex and the focus.

$$\begin{aligned}\alpha &= \arctan\left(\frac{Z_{\text{focus}}}{X_{\text{focus}}}\right)\\ \beta &= \arctan\left(\frac{Z_{\text{focus}}}{Y_{\text{focus}}}\right)\end{aligned} \tag{5}$$

3. Calculate the rotation matrix using Euler angles from the coordinates of the measured focal position.

$$\boldsymbol{R} = \begin{bmatrix} \cos(\beta) & \sin(\alpha)\sin(\beta) & \cos(\alpha)\sin(\beta) \\ 0 & \cos(\alpha) & -\sin(\alpha) \\ -\sin(\beta) & \sin(\alpha)\cos(\beta) & \cos(\alpha)\cos(\beta) \end{bmatrix} \tag{6}$$

4. Apply rotation matrix to each panel point cloud and focus point.

$$\begin{aligned}\boldsymbol{P}''_{\text{panel}} &= \boldsymbol{R}\boldsymbol{P}'_{\text{panel}}\\ \boldsymbol{P}''_{\text{focus}} &= \boldsymbol{R}\boldsymbol{P}'_{\text{focus}}\end{aligned} \tag{7}$$

5. Compare each panel to an ideal paraboloid (radius R).

$$Z_{\text{ideal}}(X,Y) = r^2/(2R) = (X^2 + Y^2)/(2R) \tag{8}$$

$$\boldsymbol{Z}_{\text{residual}}(X,Y) = Z_{\text{ideal}}(\boldsymbol{X}''_{\text{panel}}, \boldsymbol{Y}''_{\text{panel}}) - \boldsymbol{Z}''_{\text{panel}} \tag{9}$$

6. Fit residual XYZ points of each panel to a plane.

$$A\boldsymbol{X}''_{\text{panel}} + B\boldsymbol{Y}''_{\text{panel}} + C\boldsymbol{Z}_{\text{residual}} + D = 0 \tag{10}$$

7. Calculate piston, tip, and tilt from plane-fit coefficients.

$$\begin{aligned}\delta Z &= D\\ \theta &= \arctan(C/A)\\ \phi &= \arctan(C/B)\end{aligned} \tag{11}$$

The metrology process is set up to automatically deliver the required tip, tilt, and piston at the end of each measurement. Each panel has four actuators 400 mm apart in each corner, as shown in Fig. 4. Equation (12) shows how to convert the tip, tilt, and piston to the actuator number of rotations using

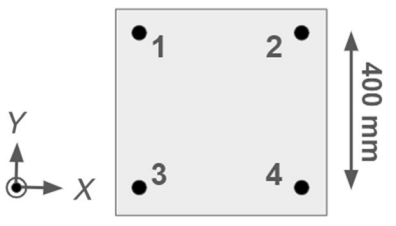

Fig. 4 Coordinate system and actuator layout for each panel. Once tip, tilt, and piston values are extracted, they must be converted to actual numbers of rotations on the actuators

the angle approximation, where δS is the spacing between actuators. Once the number of mm of translation is determined, the threads per inch (TPI) of the actuators are used to convert it to a number of rotations.

$$\begin{aligned}
\mathbf{1}&: (0.5\theta\delta S + 0.5\phi\delta S + \delta Z) * \mathrm{TPI}/25.4 \\
\mathbf{2}&: (-0.5\theta\delta S + 0.5\phi\delta S + \delta Z) * \mathrm{TPI}/25.4 \\
\mathbf{3}&: (0.5\theta\delta S - 0.5\phi\delta S + \delta Z) * \mathrm{TPI}/25.4 \\
\mathbf{4}&: (-0.5\theta\delta S - 0.5\phi\delta S + \delta Z) * \mathrm{TPI}/25.4
\end{aligned} \tag{12}$$

4 Experimental Setup, Calibration, and Configuration

4.1 Hardware

The hardware for this system uses two FLIR Blackfly S USB 3 machine vision cameras with Sony IMX183 sensors (20MP 5472x3638, with 2.4 µm pixels), each with a Computar V0826-MPZ lens (8 mm focal length). Each camera is mounted to the ends of a 0.8 m 8020 aluminum extrusion. The 8020 is mounted on a tripod for portability and pointing. With this setup, the entire 3.2 m dish can be seen from a distance of 3 ms. We used an off-axis short-throw 1080P projector from BenQ (Model MW817ST) that can cover the entire surface from a distance of 1.5 ms. The software for capturing the images, processing the fringe patterns, calculating the unwrapped phases, matching the phase pairs, and triangulating the matched pairs to produce the 3D point clouds is written in MATLAB. Photos of the camera and projector hardware are shown in Fig. 5.

4.2 Calibration

Calibration of the stereo camera pair was performed indoors for easier control of lighting and environmental conditions. An 800 mm × 600 mm aluminum and low-density polyethylene (LDPE) checkerboard calibration board with a square size of 30 mm was used. The calibration board was mounted on a tripod and traversed through the overlapping field of view (FOV) at a working distance of 3 ms for a set of 20 images. An example of one of these images is shown in Fig. 6. Using the detected checkerboard corners on each

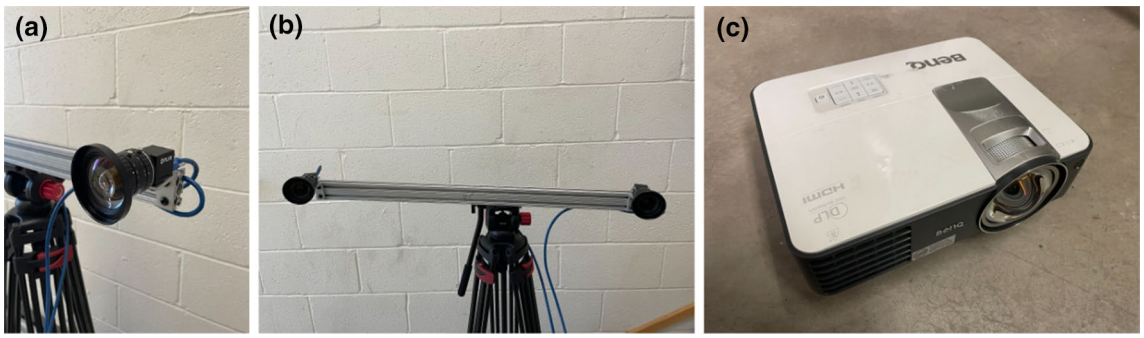

Fig. 5 **a** One of the two FLIR Blackfly USB3 cameras with an 8 mm lens. **b** Both cameras mounted to an 8020 aluminum extrusion, mounted on a tripod. **c** BenQ 1080P short-throw projector used in this experiment

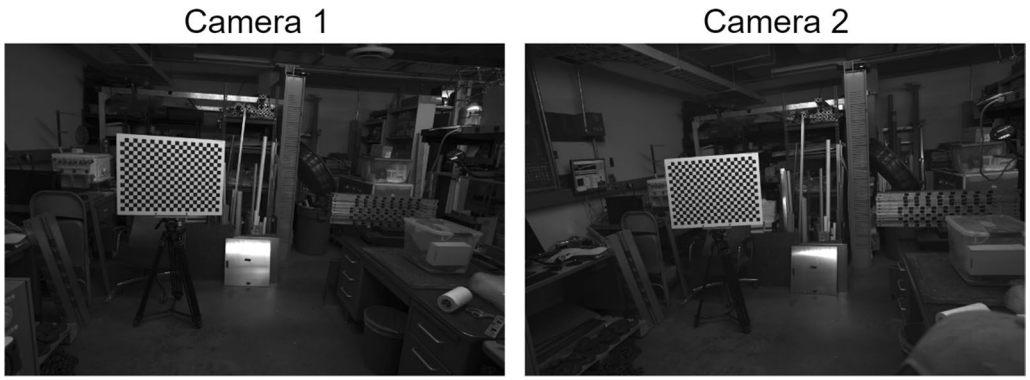

Fig. 6 An example image from the 20-image set used to calibrate the intrinsic and extrinsic parameters of the stereo camera pair. The checkerboard was moved throughout the overlapping FOV in order to properly calibrate for radial distortion

Table 1 Calibrated stereo camera parameters

Property	Camera 1	Camera 2
Focal length (pixels) f_x, f_y	3435.842, 3435.598	3439.337, 3439.499
Principle point (pixels) u_x, u_y	2745,1820	2750,1843
Radial distortion (r_2, r_4, r_6)	− .100, .126, − .043	− .096, .115, − .033
Extrinsic matrix $\begin{bmatrix} \boldsymbol{R}_{3x3} & \boldsymbol{t}_{3x1} \\ \boldsymbol{0}_{1x3} & 1 \end{bmatrix}$	$\begin{bmatrix} 0.926 & 0.061 & -0.373 & 801.048 \\ -0.072 & 0.997 & -0.014 & -40.332 \\ 0.371 & 0.039 & 0.928 & 170.496 \\ 0 & 0 & 0 & 1.0000 \end{bmatrix}$	

sensor, each camera was calibrated individually for intrinsic parameters. Then, the pair were calibrated together for extrinsic parameters, keeping the intrinsic parameters fixed. The calibrated intrinsic and extrinsic parameters are shown in Table 1.

4.3 Measurement Setup

As described in Sect. 3.2, fiducials are placed at the paraboloid vertex and the telescope focal plane to define the optical axis. The vertex and the focal plane were located using dimensions from the SRT CAD files. We placed 1.0″ white stickers in the middle of 1.5″ black stickers as reliable contrast fiducials for circle detection with the Hough transform. Figure 7 shows the physical locations of the fiducials with respect to the rest of the telescope structure and the two adjacent panels to be aligned.

Measurements of the SRT are performed at night in order to increase the SNR of the projected patterns relative

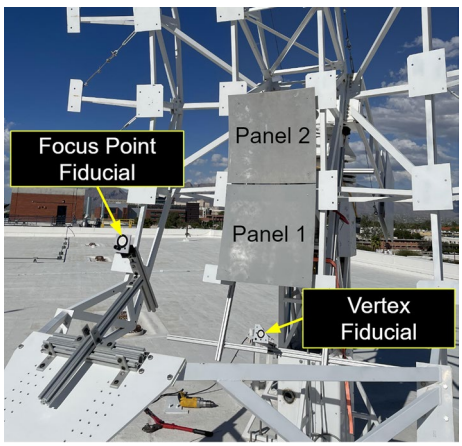

Fig. 7 Layout of the telescope structure. Two fiducials are placed where the paraboloid vertex and focus should be, using 8020 extrusions. Example Panels 1 and 2 are installed on the telescope. They are the bottom two rows of the center column of panels

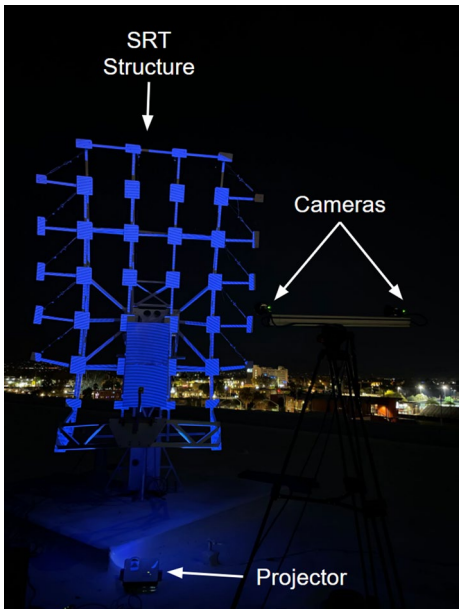

Fig. 8 Nighttime measurement setup. The projector is placed near the telescope and uses the short throw to cover the entire dish. The tripod carrying both cameras is placed roughly 3 ms away from the dish and positioned so that the entire dish can be seen in the field of view of both cameras. Shown in the image is the 10-pixel period frequency projected onto the dish structure

to ambient lighting. We also aimed for a night with low to no wind to reduce temporal errors associated with telescope structural bending or vibration. To avoid boosting noise in the images, the cameras were used with a gain of 0. To utilize the full dynamic range of the camera bitdepth, a 5-s exposure was used for each camera. As mentioned in Sect. 3.1, we employed four frequencies for the hierarchical phase unwrapping method, in which we used the N-step phase shifting algorithm [30] for each frequency and each phase shifting direction (horizontal and vertical). This results in a 40-image pattern sequence (four frequencies, five phase steps, two directions). Each pattern was captured three times and averaged to further eliminate noise, resulting in a 600-s (10-min) acquisition time. Figure 8 shows an actual data acquisition in progress at night.

Once a measurement is made, the rigid body motions for each panel are extracted using the process described in Sect. 3.2, and each panel is adjusted using four manual actuators located in the corners of each panel. The actuators have a 1 mm thread pitch and are separated by 400 mm. Thus, to tilt a panel by 1° (17.45 mrad), opposite actuators must move $\approx 400\,\text{mm} * 0.01745\,\text{rad} = 7\,\text{mm} \implies \pm 3.5\,\text{mm}$. After an iteration of adjusting the tip, tilt, and piston is performed, the panels are then remeasured, and the adjustment process is repeated until the remaining errors are corrected.

5 Results

Figure 9 shows an example set of horizontal and vertical phases from the perspectives of Camera 1 and Camera 2. Each pixel on each panel in Camera 1 has a unique combination of horizontal and vertical phases. The Camera 2 phases are searched for a matching phase pair for each pixel on Camera 1. The resulting matched locations on each camera detector are triangulated using the calibrated parameters from Table 1. Figure 10 demonstrates the data produced by the system described in this paper. Figure 10a shows the data returned from the software in its raw format, with the

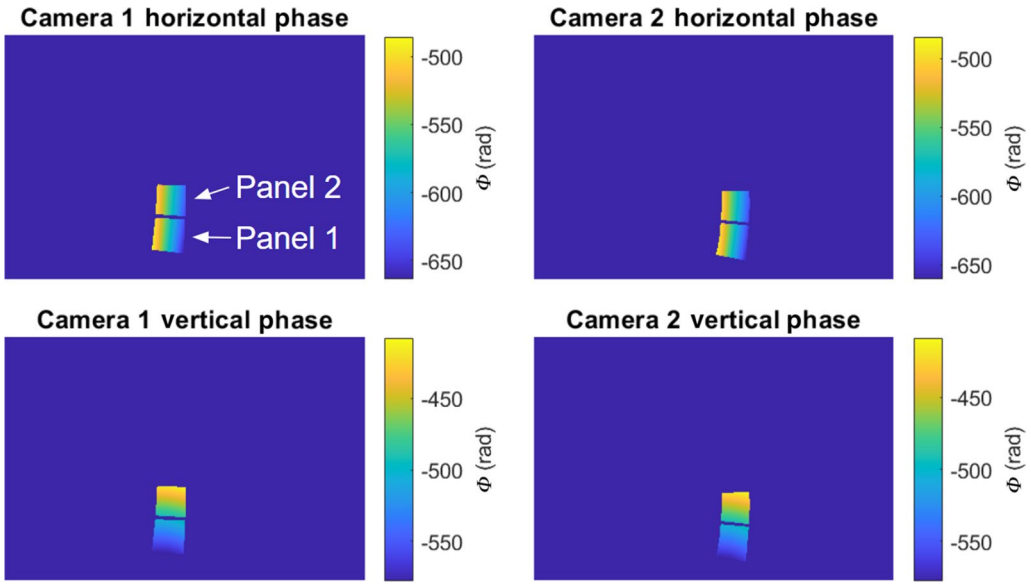

Fig. 9 Images from each camera are masked to isolate the two panels being measured. The phase unwrapping process produces four images: horizontal and vertical phase for each camera. These maps are used to find matching object locations from pixels on Camera 1 to locations on Camera 2

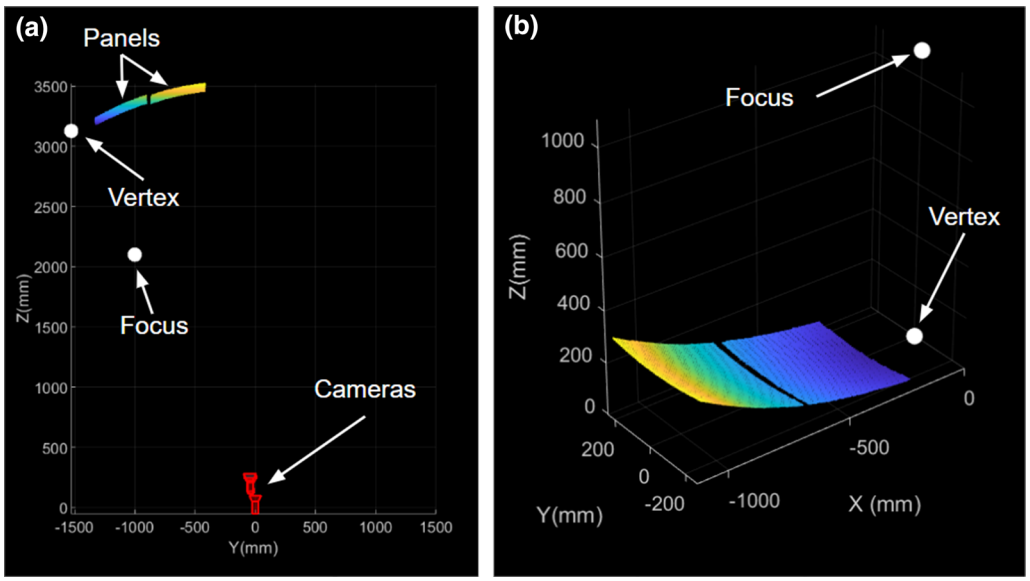

Fig. 10 Each FPP measurement results in a point cloud for each panel and the relative location of both the vertex and the focus. Raw data is shown in **a**. The triangulated 3D points are produced relative to the coordinate system defined by Camera 1. Matrix rotations and translations are applied to the panel point clouds to align the optical axis with the z-axis, shown in **b**. In this configuration, the panels can be directly compared to Eq. (9) to extract the residual error in the panels and the rigid body alignment error

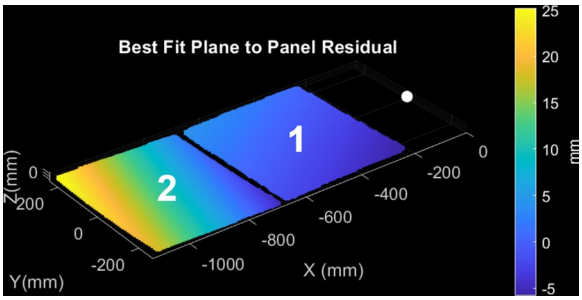

Fig. 11 Best fit planes for each panel, including piston

Table 2 Results before the first adjustment iteration

Property	Panel 1	Panel 2
δZ	− 0.70 mm	10.46 mm
θ	0.757°	0.80°
ϕ	− 0.54°	− 3.15°

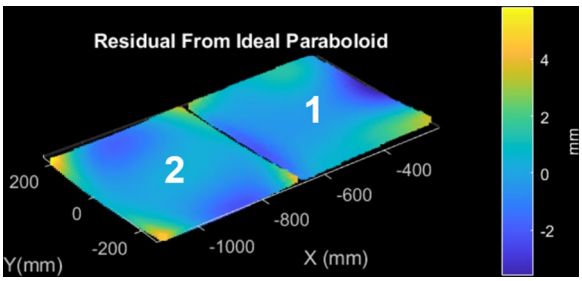

Fig. 12 In addition to finding the rigid body motion error of each panel, the system also has enough resolution to map the surface errors of each panel compared to its ideal shape. Shown here are the residual surface maps compared to the ideal paraboloid

locations of the cameras, paraboloid vertex, focus, and point clouds of both panels. Using steps 1–4 from Sect. 3.2 yields Fig. 10b to align the optical axis of the telescope with the z-axis. Steps 5–6 are followed to produce the piston, tip, and tilt error for each panel. Figure 11 shows the best fit plane for Panels 1 and 2 before adjustments begin, and Table 2 shows the actual starting piston, tip, and tilt values.

Besides the rigid body errors, each panel has imperfections relative to the ideal shape. Figure 12 shows the residual from the ideal paraboloid for each panel with tip, tilt, and piston errors removed. Panel 1 has a 1.28 mm RMS, and Panel 2 has a 0.81 mm RMS. These are not actual panels that will be used in the telescope but are examples used for this initial alignment test. For this experiment, the panel actuators on the SRT are not capable of shape correction; however, the system delivers information that could be used for this on most other large radio telescopes. The goal of the adjustment process is to make the dish surface accuracy limited by the individual panel accuracy, not the rigid body errors.

We performed four measurements with three adjustment iterations. Within three iterations, piston error was reduced to < 0.25 mm, and tip/tilt was reduced to $< 0.1°$. The final panel RMS, including alignment errors, was 1.325 mm and 0.842 mm for Panel 1 and Panel 2, respectively. Collectively, the two panels make a small dish with a 1.12 mm RMS error. Looking back at the plot of the Ruze equation in Fig. 1, this error would make the dish capable of observing 2 cm wavelengths (15 GHz) with less than 50% loss. Most of the error in this test is attributed to panel shape, which the actuators for this telescope are not configured to correct. Figure 13 shows how the piston and tip and tilt errors converged through each iteration. Table 3 shows the final adjustment results.

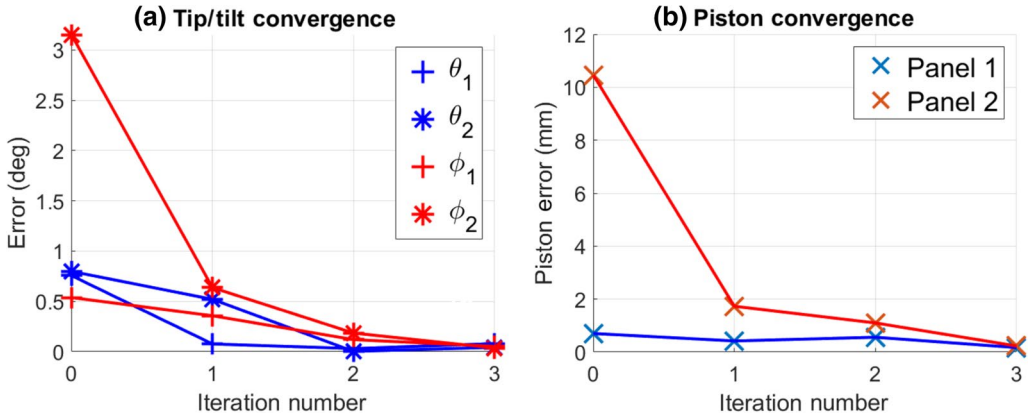

Fig. 13 Four measurements were performed, with three adjustment iterations between each measurement. **a** shows the tip and tilt of each panel improving across each iteration. **b** shows the piston for each panel also improving. Panel 1 was, fortunately, close to the ideal piston position before an adjustment was performed

Table 3 Final results after three adjustments

Property	Panel 1	Panel 2
δZ	− 0.17 mm	0.23 mm
θ	0.081°	− 0.044°
ϕ	− 0.054°	− 0.037°

Because of the premise of a large measurement area and depth variation, it is difficult to perform a direct comparison using another method to validate the accuracy of the method proposed. To understand the performance of the system, including environmental effects and structural performance, we performed three repeated measurements on the same night as the iterative alignment process. Figure 14 shows the change in the calculated tip and tilt feedback compared to the average over the three measurements, each taken every 10 min.

While this repeatability experiment does not directly establish the limitations of this metrology method, it does give insight into how the system may perform under imperfect environmental conditions. Figure 14 shows that, in the worst case, we can expect ±0.02°. Over a 500 mm panel, this is roughly ±175 µm, or 71 µm RMS. With a minimum test uncertainty ratio (TUR) of 4 to 1 [37–39], this system could be used to verify alignment to 280 µm RMS. Applying the $\lambda/15$ requirement in Fig. 1, it could be used to qualify a reflector operating at a wavelength as short as 4.2 mm or at a frequency as high as 71.4 GHz. A conservative TUR of 10 to 1 would yield a 10.5 mm wavelength or 28.6 GHz.

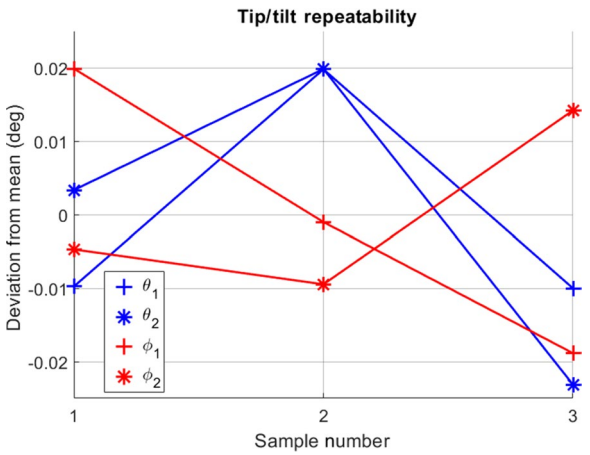

Fig. 14 Shown is the change in tip and tilt feedback for each panel compared to the average of the three measurements

6 Discussions and Future Work

This method provides several advantages over other antenna metrology methods. The major improvement results from its non-contact nature. This has a twofold benefit: speed and logistics. The setup time is less than 10 min, and the measurement takes only 10 min. Since the camera pair is pre-calibrated indoors, as shown in Fig. 6, the setup time to begin taking measurements only involves positioning the tripod so that the entire surface is in the field of view of both cameras and positioning the projector so that the entire surface is covered with projected light. During the measurement time of 10 min, the surface may vary due to environmental conditions, such as vibrations and static movements caused by wind. While this does affect the uncertainty of the measurement, it also captures the antenna performance beyond merely the surface accuracy, assuming the measurement system is stable. The acquisition time could be reduced even further by implementing a brighter projector and decreasing the required exposure time. Thanks to its rapid setup time, the system could be moved from telescope to telescope for the purpose of aligning arrays with large numbers of dishes. This would avoid the need to coordinate with satellites and the use of cryogenic detectors required by the holography method. This method also eliminates much of the manual labor required by photogrammetry and laser trackers, which require manual placement of stickers or retroreflectors. These methods are time-consuming and labor-intensive and create safety risks for workers who need to climb the dishes and place the fiducials. This method could also be installed on the telescope structure as a permanent metrology system for telescopes that have active surfaces or require regular maintenance [40]. This would also allow surface measurements to be performed at a variety of elevation angles to properly characterize gravity deformations.

Additionally, this method could be scalable to extremely large radio telescope apertures like the ngVLA 18-m dish. Sensor size, lens focal length, and the number of cameras can be adjusted to achieve the required spatial resolution and field of view to cover the aperture of a large dish. Some practical challenges related to camera calibration and projector brightness must be overcome to achieve this. Further development is needed to calibrate a large number of cameras over a large area with a long working distance. Methods that utilize auxiliary sensors to calibrate cameras with large baselines could be employed [41, 42], but they should be improved to adapt to more cameras. In addition, developing

or sourcing a projector with enough brightness to cover an area this large might be difficult. One possible solution might be found in the use of commercial cinema projectors. The authors hope that this method contributes to the development of non-contact metrology technologies needed to quickly, safely, and reliably commission large telescopes in the future.

Acknowledgements The authors would like to thank the technicians FineArc Inc for welding the structure of the SRT. The authors would also like to thank the entire team for their work in assembling the SRT structure and mounting the test panels for this experiment.

Author contributions All authors have read and accepted the final manuscript.

Funding This work was funded by the National Science Foundation (NSF) Award 2009384.

Availability of Data and Materials Data underlying the results presented in this paper are not publicly available at this time but may be obtained from the authors upon reasonable request.

Declarations

Competing interests Author Joel Berkson has a financial connection to Fringe Metrology LLC, a company that measures freeform surfaces using some of the technologies described in this paper. Justin Hyatt has a financial connection to Paramium Technologies LLC, a company that fabricates freeform curved metal surfaces. Daewook Kim is an editorial board member for "Nanomanufacturing and Metrology" and was not involved in the editorial review, or the decision to publish this article. All authors declare that there are no competing interests.

Open Access This article is licensed under a Creative Commons Attribution 4.0 International License, which permits use, sharing, adaptation, distribution and reproduction in any medium or format, as long as you give appropriate credit to the original author(s) and the source, provide a link to the Creative Commons licence, and indicate if changes were made. The images or other third party material in this article are included in the article's Creative Commons licence, unless indicated otherwise in a credit line to the material. If material is not included in the article's Creative Commons licence and your intended use is not permitted by statutory regulation or exceeds the permitted use, you will need to obtain permission directly from the copyright holder. To view a copy of this licence, visit http://creativecommons.org/licenses/by/4.0/.

References

1. Angeli GZ, Bernstein R, Walls B, et al (2018) Systems engineering for the giant magellan telescope. In: Modeling, systems engineering, and project management for astronomy VIII. SPIE, pp 203–216
2. Selina RJ, Murphy EJ, McKinnon M et al (2018) The next-generation very large array: a technical overview. In: Ground-based and airborne telescopes VII 10700, pp 497–513
3. Meinel AB (1979) Cost scaling laws applicable to very large optical telescopes. In: Crawford DL (ed), Instrumentation in astronomy III, international society for optics and photonics. SPIE, vol 0172, pp 2–7. 10.1117/12.957059
4. van Belle GT, Meinel AB, Meinel MP (2004) The scaling relationship between telescope cost and aperture size for very large telescopes. In: Ground-based telescopes, Spie, pp 563–570
5. Ruze J (1966) Antenna tolerance theory—a review. Proc IEEE 54(4):633–640
6. Baars JW, Kärcher HJ (2018) Radio telescope reflectors, vol 447. Springer, Berlin
7. Edmundson K, Baker L (2001) Photogrammetric measurement of the Arecibo primary reflector surface. In: Coordinate measurement systems committee conference
8. Li R, Qin X, Konyakhin I et al (2020) CMOS multi-matrix optoelectronic system for high speed measurement of main mirror deformation large diameter radio telescope. IEEE Access 8:51821–51829
9. Shankar NU, Duraichelvan R, Ateequlla C, et al (2009) Photogrammetric measurements of a 12-m preloaded parabolic dish antenna. arXiv:0905.1252
10. Süss M, Koch D, Paluszek H (2012) The sardinia radio telescope (SRT) optical alignment. In: Ground-based and airborne telescopes IV. SPIE, pp 843–858
11. Baars J, Martin R (1996) The Heinrich hertz telescope—a new instrument for submillimeter-wavelength astronomy. R Modern Astron 9:111–126
12. Ingalls RP, Antebi J, Ball JA et al (1994) Upgrading the haystack radio telescope for operation at 115 GHz. Proc IEEE 82(5):742–755
13. Serra G, Bolli P, Busonera G, et al (2012) The microwave holography system for the Sardinia radio telescope. In: Ground-based and airborne telescopes IV. SPIE, pp 1877–1891
14. Sullivan IS, Morales MF, Hazelton BJ et al (2012) Fast holographic deconvolution: a new technique for precision radio interferometry. Astrophys J 759(1):17
15. Cuevas LC, Alvarez ML, Leon-Huerta A, et al (2013) Iterative alignment of reflector segments using a laser tracker. In: Optical measurement systems for industrial inspection VIII. SPIE, pp 819–831
16. Leon-Huerta A, Alvarez ML, Rios EH, et al (2014) Experiences with global laser tracker alignment of the 32.5-m LMT primary surface. In: Advances in optical and mechanical technologies for telescopes and instrumentation. SPIE, pp 1244–1256
17. Wang M, Li D, Zhao Y (2020) Iterative alignment of reflector panels for large-scale compact test range in non-metrology environment based on laser tracker. Meas Sci Technol 31(4):045002
18. Attoli A, Poppi S, Buffa F, et al (2023) The Sardinia radio telescope metrology system. In: 2023 XXXVth general assembly and scientific symposium of the international union of radio science (URSI GASS). IEEE, pp 1–4
19. de Villiers MS (2023) MeerKAT Holography Measurements in the UHF, L, and S bands. Astron J 165(3):78
20. Schloerb FP, Souccar K, Gale DM, et al (2022) Lasers: a real time antenna metrology system for the large millimeter telescope. In: Advances in optical and mechanical technologies for telescopes and instrumentation V. SPIE, pp 477–488
21. Rogers AE, Barvainis R, Charpentier P et al (1993) Corrections for the effects of a Radome on antenna surface measurements made by microwave holography. IEEE Trans Antennas Propag 41(1):77–84
22. Zarghamee MS, Antebi J, Kan FW (1995) Optimal surface adjustment of haystack antenna. IEEE Trans Antennas Propag 43(1):79–86
23. de Villiers DI, Lehmensiek R (2023) Performance estimates of the 18-m ngVLA reflector system with main reflector rim extension. In: 2023 IEEE international symposium on antennas and propagation and USNC-URSI radio science meeting (USNC-URSI), IEEE, pp 763–764

24. Jewell PR (2000) The green bank telescope. Radio Telesc 4015:136–147
25. Olmi L (1998) Large millimeter telescope project: overview and optical design. Adv Technol MMW Radio Terahertz Telesc 3357:186–197
26. Theron IP, Lehmensiek R, de Villiers DI (2012) The design of the meerkat dish optics. In: 2012 international conference on electromagnetics in advanced applications. IEEE, pp 539–542
27. Berkson J, Hyatt J, Kang H et al (2023) Binocular fringe projection profilometry for the metrology of meter-scale optical surfaces. Opt. Contin. 2(4):697–711
28. Ellis W, Kim D, Hyatt J, et al (2023) Radio telescope manufacturing with adaptive aluminum thermoforming and fringe projection metrology. In: Astronomical optics: design, manufacture, and test of space and ground systems IV. SPIE, pp 195–198
29. Zhang Z (2000) A flexible new technique for camera calibration. IEEE Trans Pattern Anal Mach Intell 22(11):1330–1334
30. Zuo C, Feng S, Huang L et al (2018) Phase shifting algorithms for fringe projection profilometry: a review. Opt Lasers Eng 109:23–59
31. Su X, Chen W (2004) Reliability-guided phase unwrapping algorithm: a review. Opt Lasers Eng 42(3):245–261
32. Hartley R, Zisserman A (2003) Multiple view geometry in computer vision. Cambridge University Press, Cambridge
33. Kim EH, Hahn J, Kim H et al (2009) Profilometry without phase unwrapping using multi-frequency and four-step phase-shift sinusoidal fringe projection. Opt. Express 17(10):7818–7830
34. Zuo C, Huang L, Zhang M et al (2016) Temporal phase unwrapping algorithms for fringe projection profilometry: a comparative review. Opt Lasers Eng 85:84–103
35. Atherton TJ, Kerbyson DJ (1999) Size invariant circle detection. Image Vis Comput 17(11):795–803
36. Yuen H, Princen J, Illingworth J et al (1990) Comparative study of Hough transform methods for circle finding. Image Vis Comput 8(1):71–77
37. Delker C, Peguero I, et al (2022) A guardbanding method for managing false accept risk under process bias. Tech. rep., Sandia National Lab.(SNL-NM), Albuquerque, NM (United States)
38. Grachanen CL (2014) Calculating uncertainty. Quality Progress 47(7):44
39. Macii D, Carbone P, Petri D (2003) Management of measurement uncertainty for effective statistical process control. IEEE Trans Instrum Meas 52(5):1611–1617
40. Parker DH, Payne JM (2002) Active surface architectures of large radio telescopes. In: Proceedings of the XXVIIth URSI General Assembly in Maastricht
41. Miyata S, Saito H, Takahashi K et al (2017) Extrinsic camera calibration without visible corresponding points using omnidirectional cameras. IEEE Trans Circuits Syst Video Technol 28(9):2210–2219
42. Wang J, Guan B, Han Y et al (2023) Sensor-aided calibration of relative extrinsic parameters for outdoor stereo vision systems. Remote Sens 15(5):1300

Publisher's Note Springer Nature remains neutral with regard to jurisdictional claims in published maps and institutional affiliations.